ACS Photonics

pubs.acs.org/journal/apchd5

Article

Wideband Electrically Controlled Vernier Frequency Tunable Terahertz Quantum Cascade Laser

Iman Kundu,* Joshua R. Freeman, Paul Dean, Lianhe Li, Edmund H. Linfield, and A. Giles Davies

Cite This: *ACS Photonics* 2020, 7, 765−773

Read Online

ACCESS | Metrics & More | Article Recommendations

ABSTRACT: Frequency tuning in terahertz frequency quantum cascade lasers is challenging because of low thermal and current tuning coefficients. Moreover, photonic designs like Vernier selection based sampled gratings, used in telecom lasers to tune emission frequency, are unsuitable due to the long terahertz wavelengths and will require impractically long cavities (>15 mm). Here, we report the first wideband frequency tuning from a monolithic device exploiting Vernier selection rules using a coupled-cavity laser with a defect engineered photonic lattice. A precisely positioned defect lattice allows us to engineer the free spectral range and finesse of one of the cavities, similar to a sampled grating but using shorter cavity lengths (<4 mm). A coupled-cavity was used to tune the emission frequency. We achieve frequency tuning over 209 GHz, including mode hop-free continuous tuning of ∼6−21 GHz across six frequency bands, controlled through Stark shift, cavity-pulling, localized Joule heating, and thermal effects.

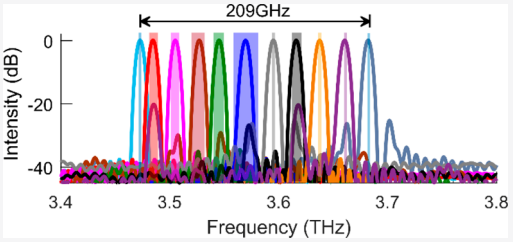

KEYWORDS: *terahertz, quantum cascade laser, frequency tuning*

Terahertz frequencies, typically referred to as the frequencies in the range 100 GHz to 10 THz, have wide range of potential applications, such as noninvasive screening, microscopy, biological sensing, medical imaging, material analysis, metrology, communications, defense, and security.[1] Advances in terahertz frequency quantum cascade lasers (QCLs)[2] over the last two decades have great potential in many of these areas. Compared to other terahertz sources, such as resonant tunneling diodes[3] and unitraveling-carrier photodiodes, these lasers offer superior performance such as multi-Watt output power,[4] ultrabroadband gain,[5,6] wide frequency range of operation (∼1.2−5.6 THz),[7,8] frequency comb operation,[9] and ultrashort pulse generation.[10]

Like most lasers, a typical QCL waveguide uses a Fabry−Pérot resonator and emits radiation at multiple cavity modes. This multimode emission property of terahertz QCLs has enabled their transition into applications such as comb spectroscopy,[9,11] but also restricts their use on other applications such as gas spectroscopy,[12,13] which require a frequency-tunable and single-mode source. Patterning of photonic structures onto the ridge waveguide has led to the realization of single-mode emission in terahertz lasers through the use of distributed feedback lattices,[14−17] photonic crystals,[18,19] and finite defect site photonic lattices.[20,21] However, tuning single mode emission in QCLs has been very difficult to achieve, restricted to a hop-free continuous frequency coverage of a maximum of ∼30 GHz,[19] limited by the weak electron plasma and band-filling effects responsible for control of the refractive index.[22]

The inherent limited current and thermal tuning coefficients in terahertz QCLs has led to the development of a number of frequency tuning techniques using external optics,[23] aperiodic lattices,[24] coupled micromirrors,[25,26] microelectromechanical actuators,[27] gas and dielectric deposition,[28,29] and facet heating.[30] However, the complex electromechanical control in some of these tuning approaches severely limits integration of the terahertz lasers into compact instrumentation systems. A terahertz laser with a monolithically integrated, electrically controlled, tuning mechanism remains an important goal for these lasers and would increase the speed of tuning, in addition to reduced system complexity and footprint.

At shorter wavelengths, lasers based on the Vernier selection of frequency are widely in telecom lasers[31] and, more recently, in mid-infrared QCLs[32] to electrically tune emission frequencies over a wide bandwidth from a monolithic device. Recently, electrically controlled frequency tuning has been realized from terahertz QCLs exploiting Vernier selection using coupled-cavities.[33−35] These lasers comprise two monolithically integrated cavities on the same substrate, which are optically coupled but electrically isolated through a narrow air gap. Each cavity supports a frequency comb of

Received: November 11, 2019
Published: February 21, 2020

https://dx.doi.org/10.1021/acsphotonics.9b01616
ACS Photonics 2020, 7, 765−773

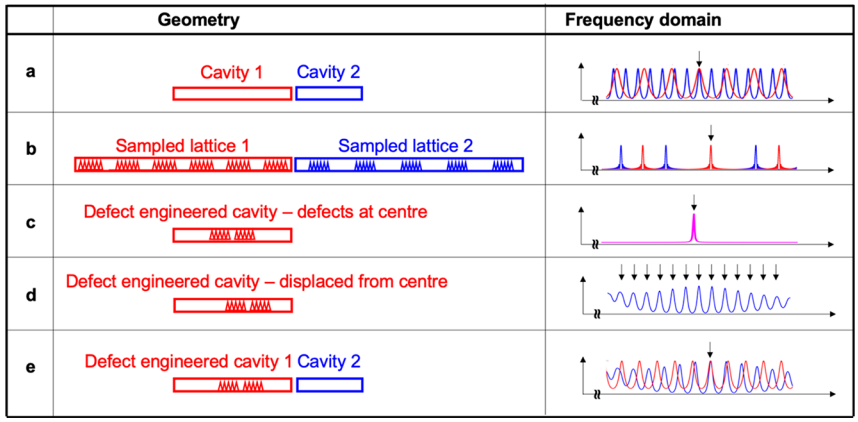

Figure 1. Schematic illustration of different laser geometries and their respective frequency characteristics. Multicavity Vernier effect based lasers: (a) coupled Fabry−Perot cavities and (b) sampled-grating distributed Bragg reflectors (SG-DBRs). The longitudinal mode spacing in coupled-cavities is controlled by changing the cavity lengths. Comb parameters (spacing, line width, finesse) in SG-DBRs are controlled by varying design parameters, such as pitch, burst period, and number of repetitions of the lattice in both cavities. Gain and phase matching sections are not shown for simplicity. (c) Single-cavity laser with a defect engineered lattice located in the center of the cavity to obtain single-mode, and (d) the same cavity with the defect engineered lattice displaced from the center to control multimode emission characteristics. (e) Defect-engineered coupled-cavities (this work). Mode spacing and finesse of the comb in one of the cavities is controlled by varying the location and spacing of defect sites etched into the cavity. The second cavity is a standard Fabry−Pérot cavity and is not etched with a lattice for simplicity.

longitudinal modes; frequency selection in such lasers is governed by the alignment between these combs. The aligned mode experiences the lowest lasing threshold, and lasing is therefore selectively favored at that frequency (Figure 1a). The emission frequency is tuned through an index perturbation in the coupled-cavities. However, the mode-spacing, line width and finesse of the combs in the individual cavities are restricted by the cavity dimensions in these simple designs, limiting tuning ranges. Alternatively, a complete control of comb parameters and wideband tuning can be designed using sampled-grating distributed Bragg reflectors (SG-DBRs), widely used in telecom lasers where they are used to achieve full coverage of the gain bandwidth through a combination of mode-hops and continuous tuning.[36] These designs are comprised of a few sections of a burst or chirped lattice on either side of a gain and a phase matching section (Figure 1b). Comb parameters, such as frequency separation and finesse, are controlled by optimizing the pitch, number of bursts, and the periodicity of the SG-DBR. A direct replication of SG-DBR Vernier designs at terahertz frequencies is not feasible because of the long wavelengths, requiring impractically long cavities extending over tens of millimeters. Instead, terahertz SG-DBRs have been applied only to single cavity QCLs and are optimized for single mode emission.[37] Although a side-mode suppression ratio of 30 dB has been reported from this design, frequency tuning from this device has not been reported.

In this work, we exploit the spectral engineering offered by defect sites in laser cavities to control comb spacing and finesse in coupled-cavity terahertz lasers. Defect sites perturb the gain in a laser cavity, resulting in a periodic modulation of the spectral envelop. A series of these defects result in a summation of all mode modulations, emanating from individual defect sites.[38,39] Traditionally, the position of the defect sites are precisely controlled to suppress longitudinal modes and to demonstrate single-mode emission, from a single laser cavity (Figure 1c).[20,39] However, there exist a tremendous flexibility for an engineering of emission characteristics of a laser cavity by simply displacing the location of the defects sites. Recently, we demonstrated the possibility of engineering emission frequencies in a single cavity terahertz QCL by simply displacing the location of a periodically arranged defect sites forming a finite photonic lattice structure. We observed switchable dual frequency operation and controlling comb spacing of longitudinal modes by simply rearranging the location of the defect sites (Figure 1d).[21] Here, we have patterned one of the cavities in a coupled-cavity terahertz QCL with a multimode defect lattice with a central π-phase shifted defect to control finesse and longitudinal mode separation (Figure 1e), much like those obtained from more complex designs such as SG-DBR but using much shorter cavities, suitable for operation at terahertz frequencies. We report both wideband mode-hops and mode-hop-free continuous tuning through Vernier selection. The emission frequencies are tuned by exploiting the Stark shift of the material gain, cavity pulling effects, localized Joule heating, and thermal coupling between cavities. We demonstrate frequency tuning over 180 GHz at a fixed heat sink temperature of 50 K. This extends to 209 GHz tuning, including mode-hop free continuous tuning over 6−21 GHz for variable heat sink temperatures. The side mode suppression ratio is in the range ∼20−40 dB. The frequency tuning range reported here is the highest obtained through electrical and thermal control in a terahertz QCL, without any external mechanical control.

DEVICE DESIGN

A coupled-cavity QCL comprising of a longer cavity (cavity 1) and a shorter cavity (cavity 2) separated by an air gap was used in this study. A schematic diagram of the terahertz QCL is shown in Figure 2. A photonic lattice was designed to be patterned on to cavity 1 only using the design methodology described in ref 21.

The design steps are (1) simulation of optical modes in the terahertz QCL with and without any cladding metal forming the photonic lattice; (2) calculation of photonic lattice periodicity as a first approximation; (3) transfer matrix simulation of the coupled-cavity QCL with and without the photonic lattice; and (4) optimization of the design using an iterative algorithm to vary the displacement and duty cycle of

https://dx.doi.org/10.1021/acsphotonics.9b01616
ACS Photonics 2020, 7, 765−773

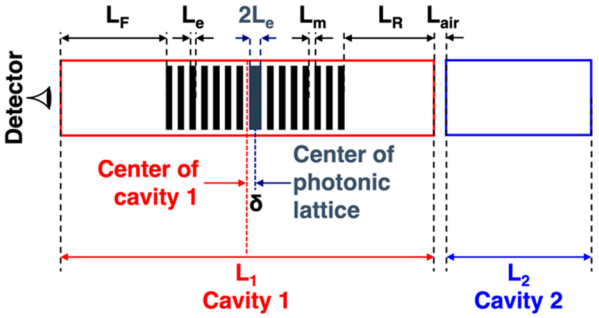

Figure 2. Schematic diagram of the coupled-cavity terahertz QCL with a defect engineered photonic lattice used in this work. The lattice is patterned on to the longer cavity (cavity 1, red). The shorter cavity (cavity 2, blue) is coupled to cavity 1 through an air-gap.

the photonic lattice to obtain a multimode the emission from cavity 1.

The optical mode in the terahertz QCL was simulated using COMSOL Multiphysics to calculate the refractive index of the fundamental mode and to design the photonic lattice to be patterned on cavity 1. A 60 μm wide narrow ridge was used to preserve the fundamental transverse mode, as well as to reduce the input electrical power to the devices. The effective refractive index of the optical mode was found to be $n_{\mathrm{eff,m}} = 3.6467$. A photonic lattice etch depth of 4 μm was computed to provide an index contrast $\Delta n_{\mathrm{eff}} = 0.6389$. The first-order Bragg wavelength (λ_{BR}) was used to calculate the lengths of the metallized (L_{m}) and the etched sections (L_{e}) of the photonic lattice as a function of the duty cycle (σ), using the following expressions:

$$L_{\mathrm{m}} = \frac{\lambda_{\mathrm{BR}}}{2}\frac{\sigma}{n_{\mathrm{eff,m}}}$$

$$L_{\mathrm{e}} = \frac{\lambda_{\mathrm{BR}}}{2}\frac{1-\sigma}{n_{\mathrm{eff,e}}}$$

In the first instance, an approximate value of the periodicity of the photonic lattice was calculated. A Bragg wavelength of $\lambda_{\mathrm{BR}} = 87.219$ μm (frequency $f_{\mathrm{BR}} = 3.437$ THz) and duty cycle of cycle $\sigma = 0.7$ was selected, resulting in calculated lengths of the metallized and the etched sections of the photonic lattice to be $L_{\mathrm{m}} = 8.37$ μm and $L_{\mathrm{e}} = 4.35$ μm, respectively. The periodicity of the photonic lattice was $\Lambda = L_{\mathrm{m}} + L_{\mathrm{e}} = 12.72$ μm.

Whereas photonic lattices are usually patterned in the center of a cavity to obtain single-mode emission, varying the position of the lattice in the cavity modifies the emission characteristics.[21] As such, the position of the lattice was displaced to modify the transmission properties of cavity 1. The transmission and spectral behavior of the coupled-cavity device with/without any photonic lattice was simulated using a transfer matrix model.

Transfer Matrix Model. The transmission characteristics of the device describing the propagation of the electric field were modeled using transfer matrices.[21,33,36] The matrix elements of a defect site are defined as

$$T_{11} = \frac{1}{t^2}[\exp(j\varphi_+) - r^2\exp(-j\varphi_-)]$$

$$T_{12} = \frac{1}{t^2}[r\exp(-j\varphi_+) - \exp(j\varphi_-)]$$

$$T_{21} = \frac{1}{t^2}[r\exp(j\varphi_+) - \exp(-j\varphi_-)]$$

$$T_{22} = \frac{1}{t^2}[\exp(-j\varphi_+) - r^2\exp(j\varphi_-)]$$

where t and r are the transmission and reflection coefficients calculated from the complex refractive indices of the fundamental mode; $\varphi_+ = \beta_{\mathrm{m}}L_{\mathrm{m}} + \beta_{\mathrm{e}}L_{\mathrm{e}}$ and $\varphi_- = \beta_{\mathrm{m}}L_{\mathrm{m}} - \beta_{\mathrm{e}}L_{\mathrm{e}}$, where β_{m} and β_{e} are complex propagation constants in the metallised and etched sections of the photonic lattice (calculated from the COMSOL model). The photonic lattice was modeled by cascading N iterations of the single defect site on either side of a central π-phase shifted defect of length $2 \times L_{\mathrm{e}}$. The center of the photonic lattice was offset from the center of cavity 1 by a distance δ, resulting in an asymmetry of the cavity 1 length on either side of the photonic lattice. We define the cavity 1 lengths from the front facet to the photonic lattice to be L_{F} and that from the lattice to the air gap to be L_{R}. The transmission through the entire device was modeled as

$$T = T_{\mathrm{F}} \times T_{\mathrm{PL}}^{N} \times T_{\mathrm{pi}} \times T_{\mathrm{PL}}^{N} \times T_{\mathrm{R}} \times T_{\mathrm{air}} \times T_2$$

where T_{F} and T_{R} are the transfer matrices of cavity 1 before and after the photonic lattice, T_{pi} is the transfer matrix of the central π-phase shifted defect of length $2 \times L_{\mathrm{e}}$, and T_{air} and T_2 are the transfer matrices of the air gap and cavity 2, respectively.

An iterative algorithm was written to systematically vary the photonic lattice parameters (L_{m}, L_{e}, and δ) and to calculate the emission properties from the device such that a multimode emission is obtained from cavity 1. In order to simulate frequency tuning properties, the transfer matrix model also included drive current dependent gain in both cavities (calculated from a Schrödinger-Poisson solver), thermal coupling between cavities (calculated using finite element modeling),[34] and waveguide dispersion.

The transfer matrix model was used to simulate emission characteristics of a 5.4 mm long QCL (with a material gain centered at ~3.55 THz[40]) that was selected for this work. An air gap was patterned using focused ion beam milling to form two optically coupled-cavities the lengths of which were selected such that the longitudinal modes from the two cavities are resonant at multiple frequencies. This was done deliberately to verify the operation of the defect engineered lattice. To achieve this, the cavity lengths were chosen to be 3.75 mm (cavity 1) and 1.65 mm (cavity 2), separated by a 10 μm wide air gap, such that the ratio between the cavity lengths is >2. Normalized transmission spectra of individual cavities are shown in Figure 3a. The transmission peaks from both cavities are spaced at a ratio of 2.27. The free spectral range of cavities 1 and 2 were calculated from the transmission peaks simulated using a transfer matrix model to be 10.89 and 24.75 GHz, respectively.

A defect engineered photonic lattice was then designed using the iterative algorithm to modify the spectral characteristics of cavity 1, and to improve the frequency emission and tuning characteristics from the device. A photonic lattice with eight defect sites on either side of a central π-phase shifted defect was designed such that a Vernier resonance is realized at the peak of the gain spectrum (~3.55 THz). For simplicity, the periodicity of the photonic lattice was kept constant at $\Lambda = 12.72$ μm, while the lattice parameters L_{m}, L_{e}, and δ were varied. The lengths of the metallized and etched sections of the

https://dx.doi.org/10.1021/acsphotonics.9b01616
ACS Photonics 2020, 7, 765−773

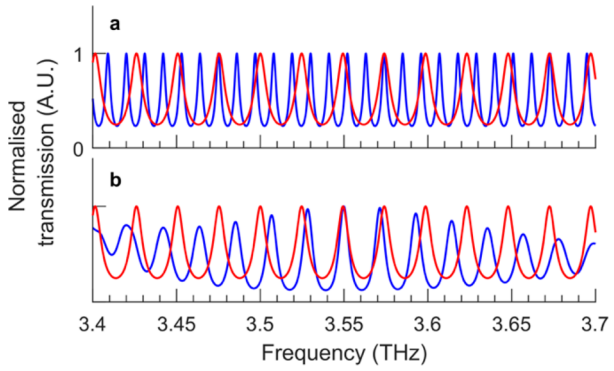

Figure 3. Simulation of transmission through the coupled-cavity QCL: (a) without any photonic lattice and (b) after patterning cavity 1 with a photonic lattice. Normalized transmission from cavities 1 and 2 are shown in blue and red, respectively.

photonic lattice required to achieve this was calculated to be $L_m = 8.9\ \mu m$ and $L_e = 3.82\ \mu m$. A central π-phase shifted defect (etched section) of length $2 \times L_e = 7.64\ \mu m$ was also included in the photonic lattice. The center of the photonic lattice was offset from the center of cavity 1 by $\delta = 36.1\ \mu m$, such that $L_F > L_R$.

Simulated normalized transmission from cavity 1 with the photonic lattice is shown in Figure 3b. The photonic lattice increases the free spectral range of cavity 1 to ~21 GHz, thereby reducing the ratio of mode separation between the cavities from 2.27 to 1.19 and disrupting the resonance at multiple frequencies so that only the resonance at ~3.55 THz remains. The finesse (F) of the cavity 1 mode at ~3.55 THz, calculated from a ratio of the free spectral range ($\Delta\lambda$) and the full-width-half-maximum bandwidth ($\delta\lambda$), increased from ~2.75 (without photonic lattice) to ~3.5 (after photonic lattice), corresponding to an increase in the reflectivity from ~36% to ~46%. In this modified coupled cavity, mode hops are expected at ~20 GHz intervals.

Frequency Tuning. The emission frequency is controlled through a combination of Stark shift of gain, cavity pulling effects, and thermal effects through localized Joule heating, thermal coupling between cavities, and by varying the heat sink temperature.

The Stark shift of the gain was calculated from the electric field (F) applied across the QCL, using the relation:[35]

$$\Delta E_S = e\Delta F(\langle \Psi_2|z|\Psi_2\rangle - \langle \Psi_1|z|\Psi_1\rangle)$$

where Ψ_1 and Ψ_2 are the wave functions of the lower and upper laser levels, calculated using a Schrödinger–Poisson solver, and e is the elementary charge. The Stark shift was calculated from the dynamic operating range of the QCL to be $\Delta E_S = 2.64$ meV, for a change in applied field $\Delta F = 6$ kV/cm (agreeing well with the reported values of 4–6 kV/cm),[40] corresponding to a change in terminal voltage of $\Delta V = 8.5$ V. From this, the Stark shift as a function of applied electric field was calculated $dE_S/dV = 0.504$ meV/V, and the coefficient of a change in refractive index is reported to be $dn/dV = 0.0021\ V^{-1}$ for the QCL material used in this study[35] and was used in the transfer matrix model.

The Stark shift arising from the diagonal transition in the QCL material allows us to further increase in tuning range by driving cavity 2 above lasing threshold and varying the gain by changing the current.[41] In this configuration, since both cavities are operating above the lasing threshold, gain is distributed between the two cavities. The frequency dependent gain in the QCL cavity results in a dispersion of the real part of the refractive index arising through Kramer–Krönig relationship.[42] This frequency-dependent dispersion was used to change the refractive index in the coupled-cavity QCL through cavity pulling effects, where the gain in cavities 1 and 2 are varied independently.[35,43] Since both cavities are driven above threshold, the perturbation of the index in the coupled-cavity QCL depends on the relative gain and Stark shift in each cavity. The dispersion at each eigenmode, simulated from the transfer matrix model, was calculated as a function of the electric field at each cavity. The amplitude of the electric field was varied throughout the dynamic range of each cavity. The change in refractive index due to the Stark shift in gain and cavity pulling was calculated to be $-14 \times 10^{-3} \leq \Delta n_C \leq 14 \times 10^{-3}$, at 3.55 THz and at a heat sink temperature of 10 K.

Refractive index was also perturbed using localized Joule heating using wide current pulses. The normalized thermal resistance of the QCL was calculated to be $R_{TH}^* = 20$ K cm W^{-1}, and the coefficient of thermal change in refractive index was calculated to be $dn/dT = 1 \times 10^{-4}\ K^{-1}$ from reference devices. A change in the refractive index of $\Delta n_T = 10 \times 10^{-3}$ was calculated when the heat sink temperature is changed by 100 K.

The change in the lattice temperature was calculated from the input electrical power and was used to estimate the change in refractive index through electrical heating. The maximum change in input electrical power during dynamic operating range for both cavities was calculated to be ~9.8 W ($\Delta V = 8.5$ V, change in drive current of 0.35 and 0.8 A for cavities 1 and 2, respectively). This results in a change of refractive index of $\Delta n_P = 18.5 \times 10^{-3}$ associated with a current pulse train with 95% duty cycle.

The transfer matrix model was modified to include refractive index perturbation through a combination of Stark shift, cavity pulling and thermal heating. To this end, the fields across both cavities were simulated to be varied across the dynamic operating range at pulse widths in the range of 2–95 μs (periodicity 100 μs), and at heat sink temperatures in the range 10–110 K. The range of refractive index change through these approaches was calculated to be $-22.5 \times 10^{-3} < \Delta n_{eff} < 22.5 \times 10^{-3}$. Emission in real experiments was collected from the front facet of cavity 1. As such, the matrix model was also modified to account for this asymmetric cavity and the additional propagation length in such drive conditions when the cavity 1 is switched off.

The simulated transmission properties from the defect engineered coupled-cavity QCL is plotted as a function of net variations ($\Delta n_{eff} = n_{eff,1} - n_{eff,2}$) in the effective refractive index (Figure 4). There are mode-hops between 8 frequency bands spanning ~3.49–3.62 THz, with a frequency separation of ~20 GHz. A mode-hop free continuous frequency tuning of ~8–13 GHz was also simulated across six of the frequency bands. The total tuning range was found to be in the range ~170–180 GHz, more than half the gain bandwidth of ~250 GHz provided by the active region in a Fabry-Pérot cavity.

FABRICATION

A terahertz QCL, based on an active region reported by Wienold et al. in ref 40 was rescaled to operate at frequencies 3.4–3.7 THz and was used for this study. The QCL was grown using molecular beam epitaxy using GaAs/$Al_{0.18}Ga_{0.82}As$ material system. Initially, a 250 nm thick GaAs buffer layer,

https://dx.doi.org/10.1021/acsphotonics.9b01616
ACS Photonics 2020, 7, 765–773

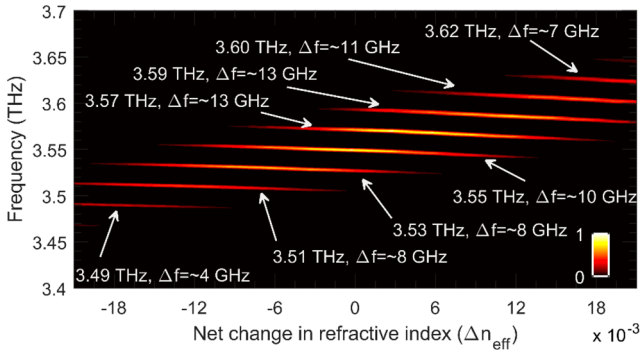

Figure 4. Simulated normalized transmission and frequency tuning range from the device as a function of total change in refractive index (controlled through a combination of Stark shift of gain, cavity pulling and thermal effects). Center frequencies and mode-hop free continuous tuning range are labeled.

and a 300 nm thick $Al_{0.5}Ga_{0.5}As$ etch stop layer was grown on top of a semi-insulating GaAs substrate. A 700 nm thick GaAs buried contact layer, *n*-doped with Si at 2×10^{18} cm^{-3} was grown next. The QCL active region was grown next, and consisted of 117 repetitions of alternating layers of $Al_{0.18}Ga_{0.82}As$/GaAs in the following sequence (starting from the injector): *3.8*/14.2/*2.9*/16.3/*2.9*/6.8/*2.9*/8.2/*2.9*/9.1/*2.9*/11.3/*1.9*/12.9/*1*/12.6/*0.5*/10.8 nm (barriers in italics). The 16.3 nm wide well (underlined) was *n*-doped with Si at 3×10^{16} cm^{-3}. Finally, a 50 nm thick *n*-doped GaAs layer, with Si doping density 5×10^{18} cm^{-3}, forming the top electrical contact was grown. QCLs with 60 μm wide semi-insulating surface plasmon waveguides were processed, as described in ref 33. A 5.42 mm long ridge was cleaved and soldered to a copper mount.

The packaged device was etched using a dual beam focused ion-beam system (FEI Nova 200 NanoLab) initially to form a 10.88 μm wide air gap separating the 3.74 mm long cavity 1 and the 1.67 mm long cavity 2. Later, a photonic lattice with $\Lambda = 12.72$ μm, $L_e = 3.82$ μm, and $L_m = 8.9$ μm was patterned using focused ion beam milling on cavity 1. The center of the photonic lattice was offset from the center of cavity 1 by 36.1 μm.

EXPERIMENTAL RESULTS

The QCL was characterized in a Janis ST-100 continuous flow helium-cooled cryostat. Both the cavities were driven with 10 kHz quasi-DC pulses with variable pulse-widths. Radiation was collected from the front facet of cavity 1 in all instances. Time averaged power was measured using a Ge:Ga photodetector and calibrated using a Thomas Keating power meter. Spectra were acquired using a Bruker Fourier transform infrared spectrometer with a resolution of 7.5 GHz. All experimental data are openly accessible from ref 44.

Power Output. The light−current−voltage characteristics of each cavity (with the other switched off) were recorded at different heat sink temperatures (Figure 5a,b). A peak output power of 3.5 and 1.25 mW was measured from cavities 1 and 2, respectively. The total output power was also measured as the current amplitudes were varied simultaneously in both cavities (Figure 5c−f). An increase in the emitted power was recorded when both cavities are driven above threshold, with a maximum power of 4 mW at a heat sink temperature of 10 K.

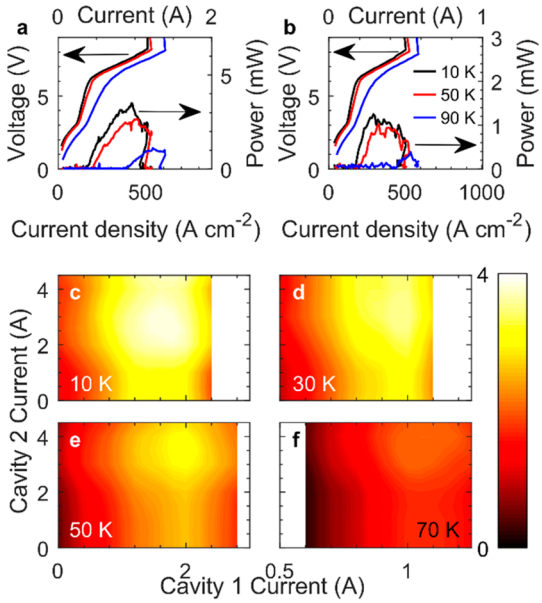

Figure 5. Power output using 2 μs wide pulses. Light−current/current density−voltage recorded from individual cavities: (a) Cavity 1 (cavity 2 off) and (b) Cavity 2 (cavity 1 off). Variation of output power as a function of drive currents in both cavities at different heat sink temperatures: (c) 10, (d) 30, (e) 50, and (f) 70 K.

Spectral Characterization. In the first instance, spectra were acquired by driving each cavity above threshold using 2 μs wide pulses, with the other cavity switched off. The single mode emission hops to higher frequencies as a function of current amplitude, due to the Stark shift of gain (Figure 6a−d). The frequency separation between the modes were measured to be in the range ∼19−20 GHz and agrees well with the simulated value of ∼20 GHz. Increasing the width of the current pulses increases the ambient lattice temperature, allowing a continuous tuning of the emission frequency in the range ∼1−1.5 GHz when pulse widths are varied in the range 2−95 μs. A variation in the peak emission frequency as a function of pulse widths at different current amplitudes and at a heat sink temperature of 70 K is shown in Figure 6e. A mode-hop free continuous tuning over ∼5−6 GHz across narrow bands of frequencies is recorded through changes in drive current amplitudes, pulse widths, and heat sink temperatures (Figure 6e,f). The results obtained here agrees well with similar results obtained from single cavity photonic lattice QCLs.[21] We note that the long electrical pulses do not result in any slow transient changes in frequency as the pulse duration used in these measurements are much longer than the time required for a single-mode to establish from transient multimodes (stabilization time of coupled-cavity terahertz QCLs are measured to be ∼1.5 ns[45]).

Spectra were similarly recorded when drive amplitude and widths of the current pulses to both cavities were varied systematically. Data recorded at a heat sink temperature of 50 K is shown in Figure 7. Mode-hop occurs between four modes when the current amplitude at cavity 2 was varied and cavity 1 was invariant (Figure 7a). The frequency tuning observed here is due to both Stark shift of gain and cavity pulling effect, and is not a superposition of emission frequencies when the cavities operated independently. This is verified by comparing the spectra to those recorded from cavity 2 alone. Frequency tuning is also controlled through thermal perturbation. Both

https://dx.doi.org/10.1021/acsphotonics.9b01616
ACS Photonics 2020, 7, 765−773

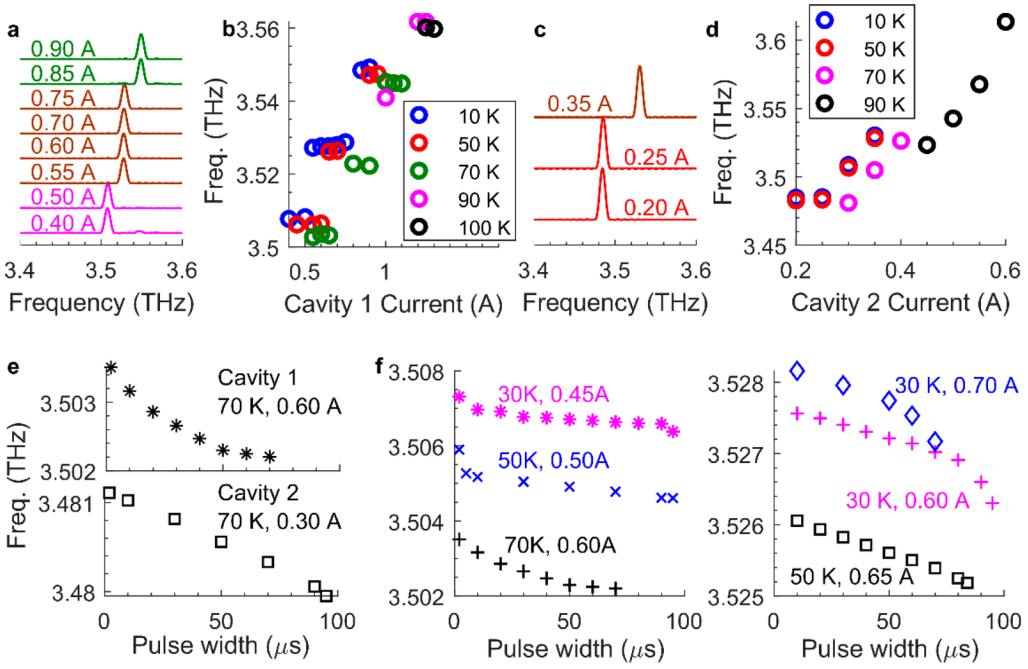

Figure 6. Spectral data recorded from individual cavities. (a) Emission spectra from cavity 1 at different current amplitudes (at 10 K). (b) Peak emission frequency as a function of cavity 1 current amplitudes at different heat sink temperatures. (c) Emission spectra from cavity 2 at different current amplitudes (at 10 K). (d) Peak emission frequency as a function of cavity 2 current amplitudes at different heat sink temperatures. (e) Continuous tuning as a function of pulse widths from individual cavities at a heat sink temperature of 70 K. (f) Representative continuous frequency tuning as a function of pulse widths from cavity 1 at different current amplitudes and heat sink temperatures from cavity 1 (centered at 3.505 and 3.5265 THz).

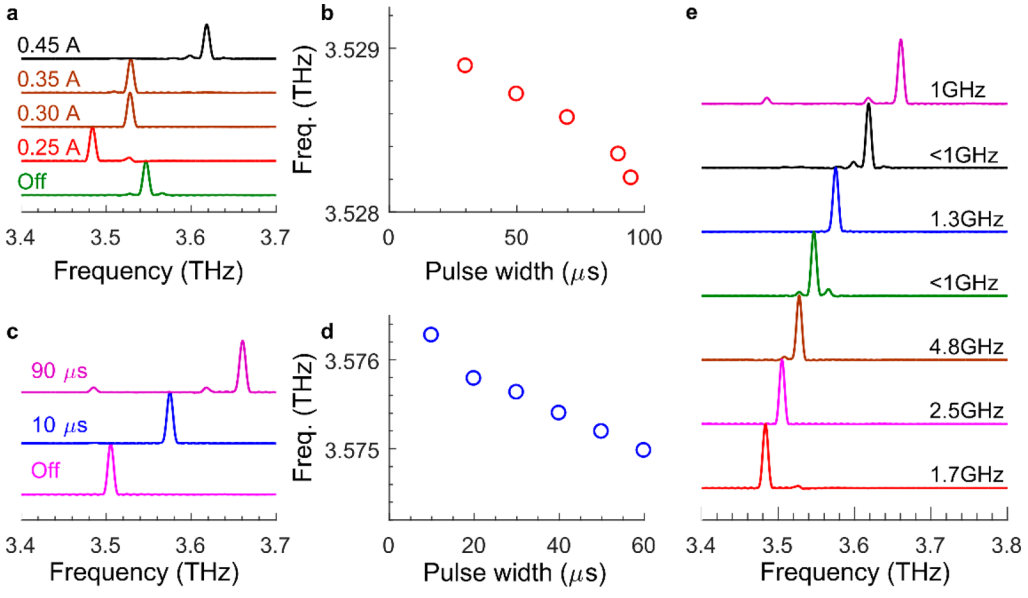

Figure 7. Spectra recorded at 50 K. (a) Frequency tuning through Stark shift and cavity pulling (using 2 μs wide pulses). Spectra recorded when cavity 1 was driven at 0.95 A and the drive currents at cavity 2 were varied. (b) Continuous frequency tuning through Joule heating by varying the current pulse widths at cavity 2. Cavity 1 is driven at 0.95 A with 2 μs wide pulses and cavity 2 is driven at 0.30 A. (c) Mode hops due to Joule heating. Cavity 1 is driven at 0.50 A and the pulse widths at cavity 2 are varied. (d) Continuous frequency tuning by varying the pulse widths at both cavities simultaneously. Both cavities are driven at 0.50 A. (e) Spectral coverage obtained by varying the electrical drive parameters systematically. Continuous tuning observed at each frequency is labeled.

mode-hops and hop-free continuous tuning was observed through a variation of pulse widths, when drive conditions in cavity 1 were invariant (Figure 7b,c). A continuous frequency tuning through thermal effects was also observed by varying pulse widths in both cavities simultaneously, while all other drive parameters remained constant (Figure 7d). Through such a systematic variation of the drive parameters, mode hops over 180 GHz (from ∼3.48−3.66 THz) and mode hop-free continuous tuning in the range ∼1−4.8 GHz was recorded at a heat sink temperature of 50 K (Figure 7e). These results are the best fast frequency tuning performance from a terahertz QCL without the need for any slow control processes like

https://dx.doi.org/10.1021/acsphotonics.9b01616
ACS Photonics 2020, 7, 765−773

changes in heat sink temperature or electromechanical optical elements. When the heat sink temperature is allowed to vary as well, the total tuning range from the device was recorded to be over 209 GHz, spanning ∼3.473−3.682 THz (Figure 8a). A

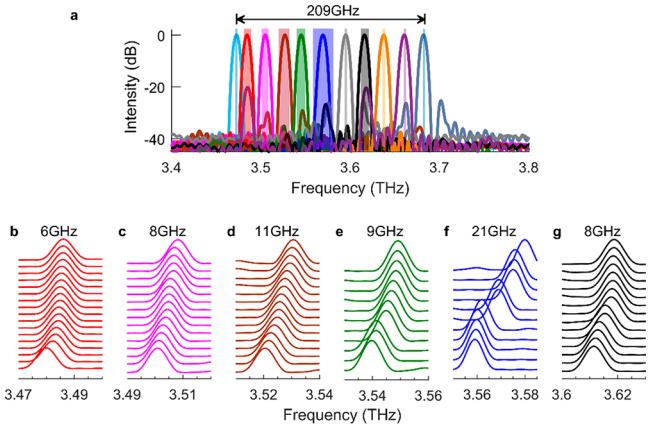

Figure 8. Complete spectral coverage from the coupled-cavity QCL. (a) Emission frequencies in the range ∼3.473−3.682 THz was recorded by varying the electrical drive parameters and the heat sink temperature between 10−110 K. Side mode suppression ratio of the emission was recorded to be in the range 20−40 dB. Mode-hop free continuous tuning range centered at each central frequency is illustrated using shaded boxes. (b−g) Mode-hop free continuous frequency tuning of ∼6, 8, 11, 9, 21, and 8 GHz recorded at frequencies ∼3.48, 3.50, 3.52, 3.54, 3.56, and 3.61 THz.

mode hop-free continuous tuning in excess of 5 GHz was recorded at center frequencies of 3.48, 3.50, 3.52, 3.54, 3.56, and 3.61 THz, over tuning ranges of ∼6, 8, 11, 9, 21, and 8 GHz, respectively (Figure 8b−g).

Although the experimentally recorded emission frequencies are ∼10 GHz lower than those simulated, the spectral coverage agrees well with the tuning range simulated from the transfer matrix model. The continuous tuning of ∼21 GHz between ∼3.56−3.58 THz shows complete frequency coverage between two discrete frequency bands and agrees well with the continuous tuning of ∼13 GHz simulated at 3.57 and 3.59 THz.

We note that frequency tuning is not controlled as a function of monotonic change of a single tuning parameter. Nevertheless, a look-up table containing peak frequencies was created to allow a programmable tuning source using appropriate instrumentation to control the electrical drive parameters, similar to the tuning control used in multisection diode lasers. While the slow heat sink temperature based control may not ideal for every application, there are many situations where frequency tuning speeds are not critical. We note that while the frequency coverage is comparable to those obtained from more advanced SG-DBR designs used in mid-infrared and diode lasers, the performance of these devices can be further improved by using a broadband QCL material[6] and coating the facets with antireflection coating.[46] We further note that the changes in drive currents to tune the emission frequency also results in a change in output power from the device, which could be mitigated by integrating an optical amplifier.[47]

Finally, although the frequency tuning reported here is predominantly based on mode-hops, a mode-hop free continuous tuning can be realized by reducing the facet reflections. However, antireflection coatings required for terahertz frequencies are more than 10 μm thick and the fabrication of such coatings are nontrivial. An alternative approach to avoid facet reflections is to couple multiple microresonators[48] using Y-branches.[35] In such a design, each microresonator can be further patterned with a photonic lattice to form a single unit repetition of a SG-DBR in a closed loop and realize a wideband continuous Vernier tunable terahertz QCL.

CONCLUSIONS

A photonic lattice is integrated on to one of the cavities in a coupled-cavity terahertz QCL to modify the comb characteristics of that cavity, similar to SG-DBR designs used in near- and mid-infrared lasers. Vernier frequency tuning from such a device is demonstrated through a combination of Stark shift, cavity pulling effect and thermal perturbation through Joule heating. Using a combination of such effects, fast frequency tuning over 180 GHz (including mode hop-free continuous tuning in the range ∼1−4.8 GHz) is demonstrated at a constant heat sink temperature of 50 K. The frequency range from the device further improved by varying the heat sink temperature to obtain a frequency tuning over 209 GHz (including continuous tuning in the range 6−21 GHz), with side mode suppression of 20−40 dB. A comprehensive database of the spectral emission was created by varying the various control parameters to build a look-up table of emission frequencies. Using this technique, the performance of devices can be further improved by using a heterogeneous active regions[49] and by coupling multiple microresonators[48] using Y-branches.[35]

AUTHOR INFORMATION

Corresponding Author

Iman Kundu − *School of Electronic and Electrical Engineering, University of Leeds, Leeds LS2 9JT, United Kingdom;* orcid.org/0000-0002-3564-1903; Email: i.kundu@leeds.ac.uk

Authors

Joshua R. Freeman − *School of Electronic and Electrical Engineering, University of Leeds, Leeds LS2 9JT, United Kingdom*

Paul Dean − *School of Electronic and Electrical Engineering, University of Leeds, Leeds LS2 9JT, United Kingdom*

Lianhe Li − *School of Electronic and Electrical Engineering, University of Leeds, Leeds LS2 9JT, United Kingdom*

Edmund H. Linfield − *School of Electronic and Electrical Engineering, University of Leeds, Leeds LS2 9JT, United Kingdom*

A. Giles Davies − *School of Electronic and Electrical Engineering, University of Leeds, Leeds LS2 9JT, United Kingdom*

Complete contact information is available at: https://pubs.acs.org/10.1021/acsphotonics.9b01616

Author Contributions

I.K. conceived and conducted the simulations, fabrication, experiments, and data analysis. E.H.L., A.G.D., and L.H.L. grew the QCL wafers. I.K., J.R.F., and P.D. wrote the manuscript with contributions from all authors. All authors have given approval to the final version of the manuscript.

https://dx.doi.org/10.1021/acsphotonics.9b01616
ACS Photonics 2020, 7, 765−773

Funding

The Engineering and Physical Sciences Research Council, UK ("COTS" and "HyperTerahertz" Programmes, EP/J017671/1 and EP/P021859/1); the Royal Society and the Wolfson Foundation.

Notes

The authors declare no competing financial interest.

■ ACKNOWLEDGMENTS

We thank A. Valavanis for proof-reading this manuscript. Research data associated with this paper are openly available from The University of Leeds data repository: http://doi.org/10.5518/757.

■ REFERENCES

(1) Dhillon, S. S.; Vitiello, M. S.; Linfield, E. H.; Davies, A. G.; Hoffmann, M. C.; Booske, J.; Paoloni, C.; Gensch, M.; Weightman, P.; Williams, G. P.; et al. The 2017 Terahertz Science and Technology Roadmap. *J. Phys. D: Appl. Phys.* **2017**, *50* (4), 043001.

(2) Köhler, R.; Tredicucci, A.; Beltram, F.; Beere, H. E.; Linfield, E. H.; Davies, A. G.; Ritchie, D. A.; Iotti, R. C.; Rossi, F. Terahertz Semiconductor-Heterostructure Laser. *Nature* **2002**, *417* (6885), 156−159.

(3) Maekawa, T.; Kanaya, H.; Suzuki, S.; Asada, M. Oscillation up to 1.92 THz in Resonant Tunneling Diode by Reduced Conduction Loss. *Appl. Phys. Express* **2016**, *9* (2), 024101.

(4) Li, L. H.; Chen, L.; Freeman, J. R.; Salih, M.; Dean, P.; Davies, A. G.; Linfield, E. H. Multi-Watt High-Power THz Frequency Quantum Cascade Lasers. *Electron. Lett.* **2017**, *53* (12), 799−800.

(5) Turčinková, D.; Scalari, G.; Castellano, F.; Amanti, M. I.; Beck, M.; Faist, J. Ultra-Broadband Heterogeneous Quantum Cascade Laser Emitting from 2.2 to 3.2 THz. *Appl. Phys. Lett.* **2011**, *99* (19), 191104.

(6) Li, L. H.; Garrasi, K.; Kundu, I.; Han, Y. J.; Salih, M. S.; Vitiello, M. S.; Davies, A. G.; Linfield, E. H. Broadband Heterogeneous Terahertz Frequency Quantum Cascade Laser. *Electron. Lett.* **2018**, *54* (21), 1229−1231.

(7) Scalari, G.; Walther, C.; Fischer, M.; Terazzi, R.; Beere, H.; Ritchie, D.; Faist, J. THz and Sub-THz Quantum Cascade Lasers. *Laser Photonics Rev.* **2009**, *3* (1−2), 45−66.

(8) Li, L.; Kundu, I.; Dean, P.; Linfield, E. H.; Davies, A. G. High-Power GaAs/AlGaAs Quantum Cascade Lasers with Emission in the Frequency Range 4.7−5.6 THz. In *International Quantum Cascade Lasers School and Workshop*; Cambridge, United Kingdom, IQCLSW, 2016; pp 87−88.

(9) Villares, G.; Hugi, A.; Blaser, S.; Faist, J. Dual-Comb Spectroscopy Based on Quantum-Cascade-Laser Frequency Combs. *Nat. Commun.* **2014**, *5*, 5192.

(10) Wang, F.; Nong, H.; Fobbe, T.; Pistore, V.; Houver, S.; Markmann, S.; Jukam, N.; Amanti, M.; Sirtori, C.; Moumdji, S.; et al. Short Terahertz Pulse Generation from a Dispersion Compensated Modelocked Semiconductor Laser. *Laser Photonics Rev.* **2017**, *11* (4), 1700013.

(11) Rösch, M.; Scalari, G.; Villares, G.; Bosco, L.; Beck, M.; Faist, J. On-Chip, Self-Detected Terahertz Dual-Comb Source. *Appl. Phys. Lett.* **2016**, *108* (17), 171104.

(12) Hübers, H.-W.; Pavlov, S. G.; Richter, H.; Semenov, A. D.; Mahler, L.; Tredicucci, A.; Beere, H. E.; Ritchie, D. A. High-Resolution Gas Phase Spectroscopy with a Distributed Feedback Terahertz Quantum Cascade Laser. *Appl. Phys. Lett.* **2006**, *89* (6), 061115.

(13) Chhantyal-Pun, R.; Valavanis, A.; Keeley, J. T.; Rubino, P.; Kundu, I.; Han, Y.; Dean, P.; Li, L.; Davies, A. G.; Linfield, E. H. Gas Spectroscopy with Integrated Frequency Monitoring through Self-Mixing in a Terahertz Quantum-Cascade Laser. *Opt. Lett.* **2018**, *43* (10), 2225−2228.

(14) Mahler, L.; Tredicucci, A.; Kohler, R.; Beltram, F.; Beere, H. E.; Linfield, E. H.; Ritchie, D. A. High-Performance Operation of Single-Mode Terahertz Quantum Cascade Lasers with Metallic Gratings. *Appl. Phys. Lett.* **2005**, *87* (18), 181101.

(15) Kumar, S.; Williams, B. S.; Qin, Q.; Lee, A. W.; Hu, Q.; Reno, J. L. Surface-Emitting Distributed Feedback Terahertz Quantum-Cascade Lasers in Metal-Metal Waveguides. *Opt. Express* **2007**, *15* (1), 113−128.

(16) Amanti, M. I.; Fischer, M.; Scalari, G.; Beck, M.; Faist, J. Low-Divergence Single-Mode Terahertz Quantum Cascade Laser. *Nat. Photonics* **2009**, *3* (10), 586−590.

(17) Jin, Y.; Gao, L.; Chen, J.; Wu, C.; Reno, J. L.; Kumar, S. High Power Surface Emitting Terahertz Laser with Hybrid Second- and Fourth-Order Bragg Gratings. *Nat. Commun.* **2018**, *9* (1), 1407.

(18) Chassagneux, Y.; Colombelli, R.; Maineult, W.; Barbieri, S.; Beere, H. E.; Ritchie, D. A.; Khanna, S. P.; Linfield, E. H.; Davies, A. G. Electrically Pumped Photonic-Crystal Terahertz Lasers Controlled by Boundary Conditions. *Nature* **2009**, *457* (7226), 174−178.

(19) Zhang, H.; Scalari, G.; Faist, J.; Dunbar, L. A.; Houdre, R. Design and Fabrication Technology for High Performance Electrical Pumped Terahertz Photonic Crystal Band Edge Lasers with Complete Photonic Band Gap. *J. Appl. Phys.* **2010**, *108* (9), 093104.

(20) Chakraborty, S.; Chakraborty, T.; Khanna, S. P.; Linfield, E. H.; Davies, A. G.; Fowler, J.; Worrall, C. H.; Beere, H. E.; Ritchie, D. A. Spectral Engineering of Terahertz Quantum Cascade Lasers Using Focused Ion Beam Etched Photonic Lattices. *Electron. Lett.* **2006**, *42* (7), 404−405.

(21) Kundu, I.; Dean, P.; Valavanis, A.; Li, L.; Han, Y.; Linfield, E. H.; Davies, A. G. Frequency Tunability and Spectral Control in Terahertz Quantum Cascade Lasers with Phase Adjusted Finite Defect Site Photonic Lattice. *IEEE Trans. Terahertz Sci. Technol.* **2017**, *7* (4), 360−367.

(22) Boylan, K.; Weldon, V.; McDonald, D.; O'Gorman, J.; Hegarty, J. Sampled Grating DBR Laser as a Spectroscopic Source in Multigas Detection at 1.52−1.57 Mm. *IEE Proc.: Optoelectron.* **2001**, *148* (1), 19−24.

(23) Lee, A. W. M.; Williams, B. S.; Kumar, S.; Hu, Q.; Reno, J. L. Tunable Terahertz Quantum Cascade Lasers with External Gratings. *Opt. Lett.* **2010**, *35* (7), 910−912.

(24) Chakraborty, S.; Marshall, O.; Hsin, C. W.; Khairuzzaman, M.; Beere, H.; Ritchie, D. Discrete Mode Tuning in Terahertz Quantum Cascade Lasers. *Opt. Express* **2012**, *20* (26), B306−B314.

(25) Castellano, F.; Bianchi, V.; Li, L.; Zhu, J.; Tredicucci, A.; Linfield, E. H.; Giles Davies, A.; Vitiello, M. S. Tuning a Microcavity-Coupled Terahertz Laser. *Appl. Phys. Lett.* **2015**, *107* (26), 261108.

(26) Curwen, C. A.; Reno, J. L.; Williams, B. S. Broadband Continuous Single-Mode Tuning of a Short-Cavity Quantum-Cascade VECSEL. *Nat. Photonics* **2019**, *13*, 855−859.

(27) Han, N.; de Geofroy, A.; Burghoff, D. P.; Chan, C. W. I.; Lee, A. W. M.; Reno, J. L.; Hu, Q. Broadband All-Electronically Tunable MEMS Terahertz Quantum Cascade Lasers. *Opt. Lett.* **2014**, *39* (12), 3480−3483.

(28) Turčinková, D.; Amanti, M. I.; Castellano, F.; Beck, M.; Faist, J. Continuous Tuning of Terahertz Distributed Feedback Quantum Cascade Laser by Gas Condensation and Dielectric Deposition. *Appl. Phys. Lett.* **2013**, *102* (18), 181113.

(29) Wu, C.; Jin, Y.; Reno, J. L.; Kumar, S. Large Static Tuning of Narrow-Beam Terahertz Plasmonic Lasers Operating at 78K. *APL Photonics* **2017**, *2* (2), 026101.

(30) Hempel, M.; Röben, B.; Schrottke, L.; Hübers, H.-W.; Grahn, H. T. Fast Continuous Tuning of Terahertz Quantum-Cascade Lasers by Rear-Facet Illumination. *Appl. Phys. Lett.* **2016**, *108* (19), 191106.

(31) Mason, B.; DenBaars, S. P.; Coldren, L. A. Tunable Sampled-Grating DBR Lasers with Integrated Wavelength Monitors. *IEEE Photonics Technol. Lett.* **1998**, *10* (8), 1085−1087.

(32) Slivken, S.; Razeghi, M. Engineering Multi-Section Quantum Cascade Lasers for Broadband Tuning. *Photonics* **2016**, *3* (3), 41.

(33) Kundu, I.; Dean, P.; Valavanis, A.; Chen, L.; Li, L.; Cunningham, J. E.; Linfield, E. H.; Davies, A. G. Discrete Vernier Tuning in Terahertz Quantum Cascade Lasers Using Coupled Cavities. *Opt. Express* **2014**, *22* (13), 16595−16605.

(34) Kundu, I.; Dean, P.; Valavanis, A.; Chen, L.; Li, L.; Cunningham, J. E.; Linfield, E. H.; Davies, A. G. Quasi-Continuous Frequency Tunable Terahertz Quantum Cascade Lasers with Coupled Cavity and Integrated Photonic Lattice. *Opt. Express* **2017**, *25* (1), 486−496.
(35) Kundu, I.; Dean, P.; Valavanis, A.; Freeman, J. R.; Rosamond, M. C.; Li, L.; Han, Y.; Linfield, E. H.; Davies, A. G. Continuous Frequency Tuning with near Constant Output Power in Coupled Y-Branched Terahertz Quantum Cascade Lasers with Photonic Lattice. *ACS Photonics* **2018**, *5* (7), 2912−2920.
(36) Coldren, L. A.; Corzine, S. W.; Masanovic, M. L. *Diode Lasers and Photonic Integrated Circuits*, 2nd ed.; Wiley Series in Microwave and Optical Engineering; John Wiley & Sons, 2012.
(37) Zhao, F.; Li, Y.; Liu, J.; Liu, F.; Zhang, J.; Zhai, S.; Zhuo, N.; Wang, L.; Liu, S.; Wang, Z. Sampled Grating Terahertz Quantum Cascade Lasers. *Appl. Phys. Lett.* **2019**, *114* (14), 141105.
(38) De Chiaro, L. F. Damage-Induced Spectral Perturbations in Multilongitudinal-Mode Semiconductor Lasers. *J. Lightwave Technol.* **1990**, *8* (11), 1659−1669.
(39) Kozlowski, D. A.; Young, J. S.; England, J. M. C.; Plumb, R. G. S. Singlemode 1.3 Mm Fabry-Perot Lasers by Mode Suppression. *Electron. Lett.* **1995**, *31* (8), 648−650.
(40) Wienold, M.; Schrottke, L.; Giehler, M.; Hey, R.; Anders, W.; Grahn, H. T. Low-Voltage Terahertz Quantum-Cascade Lasers Based on LO-Phonon-Assisted Interminiband Transitions. *Electron. Lett.* **2009**, *45* (20), 1030−1031.
(41) Qi, X.; Kundu, I.; Dean, P.; Agnew, G.; Taimre, T.; Valavanis, A.; Grier, A. T.; Linfield, E. H.; Davies, A. G.; Indjin, D.; Rakic, A. D.; et al. Mode Selection and Tuning Mechanisms in Coupled-Cavity Terahertz Quantum Cascade Lasers. *IEEE J. Sel. Top. Quantum Electron.* **2017**, *23* (4), 1−12.
(42) Yariv, A. *Quantum Electronics*, 3rd ed.; John Wiley & Sons, 1988.
(43) Turčinková, D.; Amanti, M. I.; Scalari, G.; Beck, M.; Faist, J. Electrically Tunable Terahertz Quantum Cascade Lasers Based on a Two-Sections Interdigitated Distributed Feedback Cavity. *Appl. Phys. Lett.* **2015**, *106* (13), 131107.
(44) Kundu, I.; Freeman, J. R.; Dean, P.; Li, L.; Linfield, E. H.; Davies, A. G. *Data Associated with "Wideband Electrically-Controlled Vernier Frequency Tuneable Terahertz Quantum Cascade Laser"*. University of Leeds data repository, 2020.
(45) Kundu, I.; Wang, F.; Qi, X.; Nong, H.; Dean, P.; Freeman, J. R.; Valavanis, A.; Agnew, G.; Grier, A.; Taimre, T.; et al. Ultrafast Switch-on Dynamics of Frequency Tuneable Semiconductor Lasers. *Nat. Commun.* **2018**, *9* (1), 3076.
(46) Kalchmair, S.; Blanchard, R.; Mansuripur, T. S.; de Naurois, G.-M.; Pfluegl, C.; Witinski, M. F.; Diehl, L.; Capasso, F.; Loncar, M. High Tuning Stability of Sampled Grating Quantum Cascade Lasers. *Opt. Express* **2015**, *23* (12), 15734−15747.
(47) Zhu, H.; Wang, F.; Yan, Q.; Yu, C.; Chen, J.; Xu, G.; He, L.; Li, L.; Chen, L.; Davies, A. G.; et al. Terahertz Master-Oscillator Power-Amplifier Quantum Cascade Lasers. *Appl. Phys. Lett.* **2016**, *109* (23), 231105.
(48) Kundu, I.; Freeman, J. R.; Dean, P.; Li, L. H.; Linfield, E. H.; Davies, A. G. Terahertz Photonic Integrated Circuit for Frequency Tuning and Power Modulation. *Opt. Express* **2020**, *28* (2), 4374−4386.
(49) Khanna, S. P.; Salih, M.; Dean, P.; Davies, A. G.; Linfield, E. H. Electrically Tunable Terahertz Quantum-Cascade Laser with a Heterogeneous Active Region. *Appl. Phys. Lett.* **2009**, *95* (18), 181101−181103.

https://dx.doi.org/10.1021/acsphotonics.9b01616
ACS Photonics 2020, 7, 765−773